The Astrophysical Journal, 911:144 (15pp), 2021 April 20 https://doi.org/10.3847/1538-4357/abec82

GASP XXXIV: Unfolding the Thermal Side of Ram Pressure Stripping in the Jellyfish Galaxy JO201

M. Giulia Campitiello[1,2], Alessandro Ignesti[1,3], Myriam Gitti[1,4], Fabrizio Brighenti[1,5], Mario Radovich[3], Anna Wolter[6], Neven Tomičić[3], Callum Bellhouse[3,7], Bianca M. Poggianti[3], Alessia Moretti[3], Benedetta Vulcani[3], Yara L. Jaffé[8], Rosita Paladino[4], Ancla Müller[9], Jacopo Fritz[10], Ana C. C. Lourenço[8], and Marco Gullieuszik[3]
[1] Dipartimento di Fisica e Astronomia, Università di Bologna, via Piero Gobetti 93/2, I-40129 Bologna, Italy; maria.campitiello2@unibo.it
[2] INAF, Osservatorio Astronomico di Bologna, via Piero Gobetti, 93/3, 40129 Bologna, Italy
[3] INAF-Padova Astronomical Observatory, Vicolo dell'Osservatorio 5, I-35122 Padova, Italy
[4] INAF, Istituto di Radioastronomia di Bologna, via Piero Gobetti 101, I-40129 Bologna, Italy
[5] Department of Astronomy and Astrophysics, University of California, 1156 High Street, Santa Cruz, CA 95064, USA
[6] INAF-Osservatorio Astronomico di Brera, via Brera 28, I-20121 Milano, Italy
[7] University of Birmingham School of Physics and Astronomy, Edgbaston, Birmingham B15 2TT, England
[8] Instituto de Física y Astronomía, Universidad de Valparaíso, Avda. Gran Bretaña 1111 Valparaíso, Chile
[9] Ruhr University Bochum, Faculty of Physics and Astronomy, Astronomical Institute, Universitätsst 150, D-44801 Bochum, Germany
[10] Instituto de Radioastronomía y Astrofísica, UNAM, Campus Morelia, A.P. 3-72, C.P. 58089, Mexico
Received 2021 January 30; revised 2021 March 1; accepted 2021 March 5; published 2021 April 28

Abstract

X-ray studies of jellyfish galaxies play a crucial role in understanding the interactions between the interstellar medium (ISM) and the intracluster medium (ICM). In this paper, we focused on the jellyfish galaxy JO201. By combining archival Chandra observations, Multi Unit Spectroscopic Explorer Hα cubes, and maps of the emission fraction of the diffuse ionized gas, we investigated both its high-energy spectral properties and the spatial correlation between its X-ray and optical emissions. The X-ray emission of JO201 is provided by both the Compton-thick active galactic nucleus ($L_{\rm X}^{0.5-10{\rm keV}} = 2.7 \cdot 10^{41}$ erg s^{-1}, not corrected for intrinsic absorption) and an extended component ($L_{\rm X}^{0.5-10\,{\rm keV}} \approx 1.9$–$4.5 \cdot 10^{41}$ erg s^{-1}) produced by a warm plasma ($kT \approx 1$ keV), whose luminosity is higher than expected from the observed star formation ($L_{\rm X} \sim 3.8 \cdot 10^{40}$erg s^{-1}). The spectral analysis showed that the X-ray emission is consistent with the thermal cooling of hot plasma. These properties are similar to the ones found in other jellyfish galaxies showing extended X-ray emission. A point-to-point analysis revealed that this X-ray emission closely follows the ISM distribution, whereas CLOUDY simulations proved that the ionization triggered by this warm plasma would be able to reproduce the [O I]/Hα excess observed in JO201. We conclude that the galactic X-ray emitting plasma originates on the surface of the ISM as a result of the ICM–ISM interplay. This process would entail the cooling and accretion of the ICM onto the galaxy, which could additionally fuel the star formation, and the emergence of [O I]/Hα excess in the optical spectrum.

Unified Astronomy Thesaurus concepts: Galaxy evolution (594); X-ray astronomy (1810); Galaxy clusters (584)

1. Introduction

The evolution of galaxies is strongly influenced by all those phenomena that can alter their gas content. Due to internal processes, like feedback from supernovae (SN) and active galactic nuclei (AGNs; e.g., Ho et al. 2014), or external processes, like harassment (e.g., Moore et al. 1998), strangulation (e.g., Larson et al. 1980), and tidal interactions (e.g., Springel 2000), galaxies can either acquire gas, increasing their star formation (SF), or, loose their gas, turning into passive systems (e.g., van Gorkom 2004, and references therein). One of the main processes involved in removing gas from galaxies is ram pressure stripping (RPS). This mechanism was proposed for the first time by Gunn et al. (1972) to explain the lack of gas-rich galaxies in clusters. Any time a galaxy falls into the intracluster medium (ICM), it experiences a force in the opposite direction of its relative motion. If this force overcomes the gravitational one, the gas component is stripped away, causing a transformation that can turn the galaxy into a quenched system. The condition for gas loss is given by $\rho_{\rm ICM} v_{\rm in}^2 > 2\pi G \Sigma_{\rm s} \Sigma_{\rm g}$, that is, when the ram pressure is higher than the gravitational pressure. Here $\Sigma_{\rm s}$ and $\Sigma_{\rm g}$ are, respectively, the surface density of stars and gas, $\rho_{\rm ICM}$ is the ICM mass density, and $v_{\rm in}$ is the infall velocity of the galaxy. Starting from this relation, it is possible to identify regions of the phase-space diagram in which the stripping process is heavily favored; they are characterized by small cluster radii (where the ICM density is higher) and high galaxy velocity (Jaffé et al. 2015, 2016; Yoon et al. 2017). In these regions in particular, the presence of peculiar galaxies was observed: these objects show clear signs of the ongoing stripping process, i.e., tails or "tentacles" of diffuse gas extended in the opposite direction of the galaxy motion (Jaffé et al. 2018; Gullieuszik et al. 2020). The most extreme examples of galaxies undergoing strong ram pressure are the so-called jellyfish galaxies (Smith et al. 2010; Ebeling et al. 2014; Fumagalli et al. 2014; Poggianti et al. 2017b), objects that show extra-planar, unilateral debris visible in the optical/UV light and striking tails of Hα ionized gas.

Jellyfish galaxies represent the transitional phase between infalling star-forming spirals and quenched cluster early-type galaxies, and they provide a unique opportunity to understand the impact of gas removal processes on both the SF and the AGN activity. One of the most recent research projects in this field is GAs Stripping Phenomena (GASP), a European Southern Observatory (ESO) Large Program carried out with the Multi Unit Spectroscopic Explorer (MUSE) at the Very Large Telescope (VLT), to observe 94 stripping candidates at

$z = 0.04$–0.07 (Poggianti et al. 2017b). These galaxies were selected by visual inspection based on the presence of RPS signatures, such as displaced tails and asymmetric morphologies, from the WIdefield Nearby Galaxy-cluster Survey (WINGS; Fasano et al. 2006; Moretti et al. 2014), its extension OmegaWINGS (Gullieuszik et al. 2015; Moretti et al. 2017), and the Padova-Millennium Galaxy and Group Catalogue (Calvi et al. 2011).

To investigate the effects and the features of such a complex process as the RPS, multiwavelength studies are required. With this approach, it is in fact possible to observe the different phases of the stripped gas (e.g., Poggianti et al. 2019b), to reconstruct the SF history of the galaxy (visible in the optical band; e.g., Bellhouse et al. 2019), and to understand the impact of the magnetic fields on the stripping process (visible in the radio band; e.g., Müller et al. 2021). However, the high-energy side of jellyfish galaxies is still deeply unexplored, with only a few objects studied in detail: ESO 137-001 and ESO 137-002 in A3627 (Sun et al. 2010; Zhang et al. 2013), the GASP galaxy JW100 in A2626 (Poggianti et al. 2019b), NGC 6872 in the galaxy group Pavo (Machacek et al. 2005), NGC 4569 in Virgo (Tschöke et al. 2001), and UGC 6697 in A1367 (Sun & Vikhlinin 2005). However, for the latter three galaxies, a further contribution arising from tidal interactions cannot be completely excluded. These studies found that the galactic extended X-ray emission is produced by a warm plasma with a temperature in the range $kT \sim 0.7$–1 keV, likely originating from the interplay between the interstellar medium (ISM) and the ICM on the surface of the stripped tails. From the analysis of JW100, it was observed that the star formation rate (SFR) is not able to explain the observed X-ray luminosity of the galaxy and, thus, an additional emission mechanism is required. Moreover, a spatial correlation between X-ray and Hα surface brightness was found and was interpreted as evidence of the strict connection between the X-ray emitting plasma and the ISM. Based on these results and on previous studies about the phase transformation of the ram pressure stripped gas through shocks, heat conduction, magnetohydrodynamic waves, and turbulence (e.g., Cowie & Songaila 1977; Nulsen 1982; Gavazzi et al. 2001; Sun et al. 2006, 2007, 2010; Boselli et al. 2016; Fossati et al. 2016), it was argued that the origin of the extended X-ray emission observed in jellyfish galaxies could be related to the ongoing stripping process. The X-ray emitting plasma would then be the result of the complex ICM–ISM interaction triggered by the stripping, which causes either the heating of the ISM through shocks and conduction, or the cooling of the ICM onto the galaxy or the ICM–ISM mixing.

With the aim to expand the sample of jellyfish galaxies with detailed X-ray analysis, and with the purpose of addressing the open questions triggered by the JW100 study, we carried out an X-ray investigation of another jellyfish galaxy of the GASP sample, JO201. This galaxy has been extensively studied at many wavelengths (e.g., Bellhouse et al. 2017, 2019, 2021; George et al. 2018; Moretti et al. 2020; Ramatsoku et al. 2020) and disposes of deep, archival Chandra observations, necessary for a detailed X-ray analysis. This paper is structured as follows. In Section 2 we present the main properties of JO201 and its host cluster A85. In Section 3 we describe the procedures adopted for the Chandra data reduction and extraction of spectra. In Section 4 we present the results of our detailed spectral analysis, and discuss them in Section 5. Conclusions are presented in Section 6. Throughout this paper, we assume $H_0 = 70\,\mathrm{km\,s^{-1}\,Mpc^{-1}}$, $\Omega_M = 0.3$, and $\Omega_\Lambda = 0.7$ ($1'' = 1.085$ kpc at $z = 0.05586$), and errors are given at the 1σ level.

2. JO201 and the Cluster A85

As mentioned in the Introduction, to fully understand the ongoing stripping process in JO201, it is necessary to use a multiwavelength approach and to take into account the properties of the environment in which the galaxy is located. For this reason, we briefly present in the following subsection the results of previous studies of both JO201 and its host cluster Abell 85 (A85).

2.1. The Galaxy Cluster A85

A85 ($z = 0.05586$ and $M_{200} = 1.58 \cdot 10^{15}\,M_\odot$; Moretti et al. 2017) is one of the brightest galaxy clusters in the X-ray sky (Edge et al. 1990) and hosts the largest brightest central galaxy (BCG) ever observed in the optical band (López-Cruz et al. 2014), namely Holm 15A. Despite being classified as a cool-core cluster, A85 is undergoing a merger with two subclusters: one from the south and the other one from the southwest. In order to investigate the peculiar dynamical state of A85, Ichinohe et al. (2015) analyzed its X-ray emission by means of a deep Chandra exposure. This analysis highlighted the presence of an apparent brightness excess spiral, starting north of the core and extending counterclockwise outward from the core out to ~600 kpc. This feature is attributable to the sloshing of the ICM in the gravitational potential of the cluster triggered by previous merger events. Furthermore, it was observed that the southern subcluster core is almost entirely stripped of the low-entropy gas, providing a case of efficient destruction of a cool core during a merger. Starting from the X-ray spectral analysis, radial profiles of the thermal properties of the cluster were derived. According to them, in the annular region between $r_1 = 200$ kpc and $r_2 = 400$ kpc, where JO201 is located, a temperature of $kT \simeq 6.7$ keV, a density of $n_e \simeq 10^{-3}\,\mathrm{cm^{-3}}$, and an ICM pressure of $p \simeq 10^{-2}\,\mathrm{keV\,cm^{-3}}$ were measured.

2.2. JO201: The Current State of the Art

JO201 is a Seyfert 2 galaxy (R.A. 00:41:30.325, decl. -09:15:45.96; Bellhouse et al. 2017) located at a distance of 360 kpc northwest from the BCG (R.A. 00:41:50.54, decl. −09:18:13.07; Edwards et al. 2016). It is characterized by a stellar mass of $M_s = 3.55^{+1.24}_{-0.23} \cdot 10^{10}\,M_\odot$ and a line-of-sight velocity of $v = 3363.7$ km s^{-1} with respect to the mean velocity of the cluster (Bellhouse et al. 2017; Vulcani et al. 2018). Its proximity to the center of A85, along with its very high velocity, make the stripping process extremely efficient. Referring to the main questions that the GASP project aims to answer (Poggianti et al. 2017b), in this subsection we present both the results obtained from previous optical and radio studies of JO201 and the open questions.

1. For how long, where, and why does gas removal occur? The motion of JO201 develops almost exclusively along the line of sight in the direction of the observer, providing a unique perspective on the stripping process. The orientation of the galaxy is indeed face-on, and the interaction with the ICM occurs frontally. This allows us to recognize a particular pattern in the distribution of the

Hα emission attributable to the unwinding of the spiral arms (Bellhouse et al. 2021). Observations revealed that the efficiency of the stripping is such that gas was removed even from the innermost part of the stellar disk. From *N*-body simulations, it was estimated that the process has been ongoing for ∼0.6–1.2 Gyr, and thus a long extension of the gas tail is expected (Bellhouse et al. 2019). Hα observations highlight the presence of gas up to a distance of 50 kpc from the disk, but this value could be underestimated due to the particular orientation of JO201. For this reason, Bellhouse et al. (2019) resorted to simulations to investigate the motion and dynamics of a cloud of gas that is accelerated away from the galaxy, after being stripped by ram pressure, finding that the real length of the tail is probably ∼94 kpc.

2. What is the impact of the RPS process on SF? Previous studies found that JO201 has a total integrated SFR of $6 \pm 1\ M_{\odot}\ \mathrm{yr}^{-1}$, which is 0.4–0.5 dex above the main sequence of non-stripped disk galaxies (Vulcani et al. 2018), and shows a molecular gas content four to five times higher than normal galaxies of similar mass (Moretti et al. 2020). In particular, the neutral gas mass (H I) is 14 times lower than the molecular gas mass (H_2), which is in contrast with the behavior of normal spiral galaxies. The hypothesis suggested until now to interpret these features is that ram pressure could be able to compress the gas, increasing the SF and converting H I into H_2 effectively (Ramatsoku et al. 2020).
3. What is the impact of the AGN activity on the RPS process? JO201 hosts an AGN whose activity influenced the central region, both ionizing the surrounding gas (Poggianti et al. 2017b; Bellhouse et al. 2019; Radovich et al. 2019) and quenching the SF (George et al. 2019). However, a detailed analysis of its X-ray emission has not been carried out yet.

Therefore, it clearly appears that there are still several shortcomings in the understanding of the ongoing stripping process in JO201, regarding the nature of the interaction between the ISM and the ICM, and the properties of the AGN. In this paper, we aim at investigating the origin of the extended X-ray emission associated with JO201, by means of a dedicated reanalysis of the archival Chandra observations (first presented by Ichinohe et al. 2015). In particular, we aim at discerning if the X-ray emission is linked to the intense ongoing SF or to a further contribution caused by the RPS process and also at analyzing the AGN, in order to understand the origin of its high-energy emission.

3. Data Analysis

3.1. Chandra Data Processing

We analyzed archival Chandra observations of the cluster A85 consisting of five different exposures (ObsID 15173, 15174, 16263, 16264, and 904; see Table 1) hosting the galaxy JO201. Each observation was obtained with the ACIS-I instrument in the VFAINT mode, and the cluster emission extends over all four chips. Data were downloaded from the Chandra Data Archive[11] and were reprocessed with the software package CIAO (version 4.11) and CALDB (version 4.8.3) to apply the latest calibration and to remove bad pixels and flares. The net exposure times obtained after this phase of data cleaning are summarized in Table 1. We also improved the absolute astrometry identifying the point sources with the task `WAVDETECT` and cross-matching them with the optical catalog USNO-A2.0.[12] For background subtraction, we first identified and re-projected the ACIS background files (`blanksky`) that match our data. Then we treated each chip of each `blanksky` separately, normalizing them to the count rate of the corresponding chip of the source image in the 9–12 keV band.

Table 1
Summary of the Observations: Net Exposure Times Are the Values after Cleaning

ObsID	Date time (ks)	Net Exposure	PI
15173	2013-08-14	40.2	S. Allen
15174	2013-08-09	38.2	S. Allen
16263	2013-08-10	36.3	S. Allen
16264	2013-08-17	34.3	S. Allen
904	2000-08-19	37.9	C.L. Sarazin

For each observation, we produced an image in units of counts (`counts/pixel`), an exposure map (`cm`^{2}`·s·counts/photons`) and an image in units of flux (`photons/(cm`^{2}`·s·pixel)`) resulting from the division between the image in units of counts and the exposure map. Combining the five images in units of flux and filtering data in the 0.5–2.0 keV band, we produced the exposure-corrected mosaic shown in Figure 1.

3.2. X-Ray Morphology

From the exposure-corrected mosaic (Figure 1), it is possible to recognize the main features of the cluster A85 presented in Section 2.1. In particular, in the southern and southwestern regions, we identify the two subclusters that are falling toward the center of A85. Despite the presence of these two mergers, the gas distribution follows a spherical symmetry elsewhere in the cluster.

To the northwest of the BCG, in correspondence to the position of JO201, it is possible to observe an extended X-ray emission. Specifically, we distinguish a central region related to the center of the galaxy disk including the AGN and a southern, arcuate region resembling the unwinding of the spiral arm (Bellhouse et al. 2021). The X-ray emission is less extended than the optical disk, but, as in the case of JW100 (see Section 1), it coincides spatially with the Hα emission (see also Figure 6).

3.3. Point-to-point Analysis

In order to unfold the connection between the X-ray emitting plasma and the galactic warm gas, we carried out a point-to-point study of the spatial correlation between the two respective emissions, i.e., X-rays and Hα.

We combined the Chandra image with MUSE Hα cubes and emission fraction of the diffuse ionized gas (DIG) maps (Reynolds 1985; Haffner et al. 1999; Reynolds et al. 1999; Tomičić et al. 2021). The Hα observations of JO201 were taken as part of the GASP program with the MUSE integral

[11] https://cda.harvard.edu/chaser/

[12] http://tdc-www.harvard.edu/catalogs/ua2.html

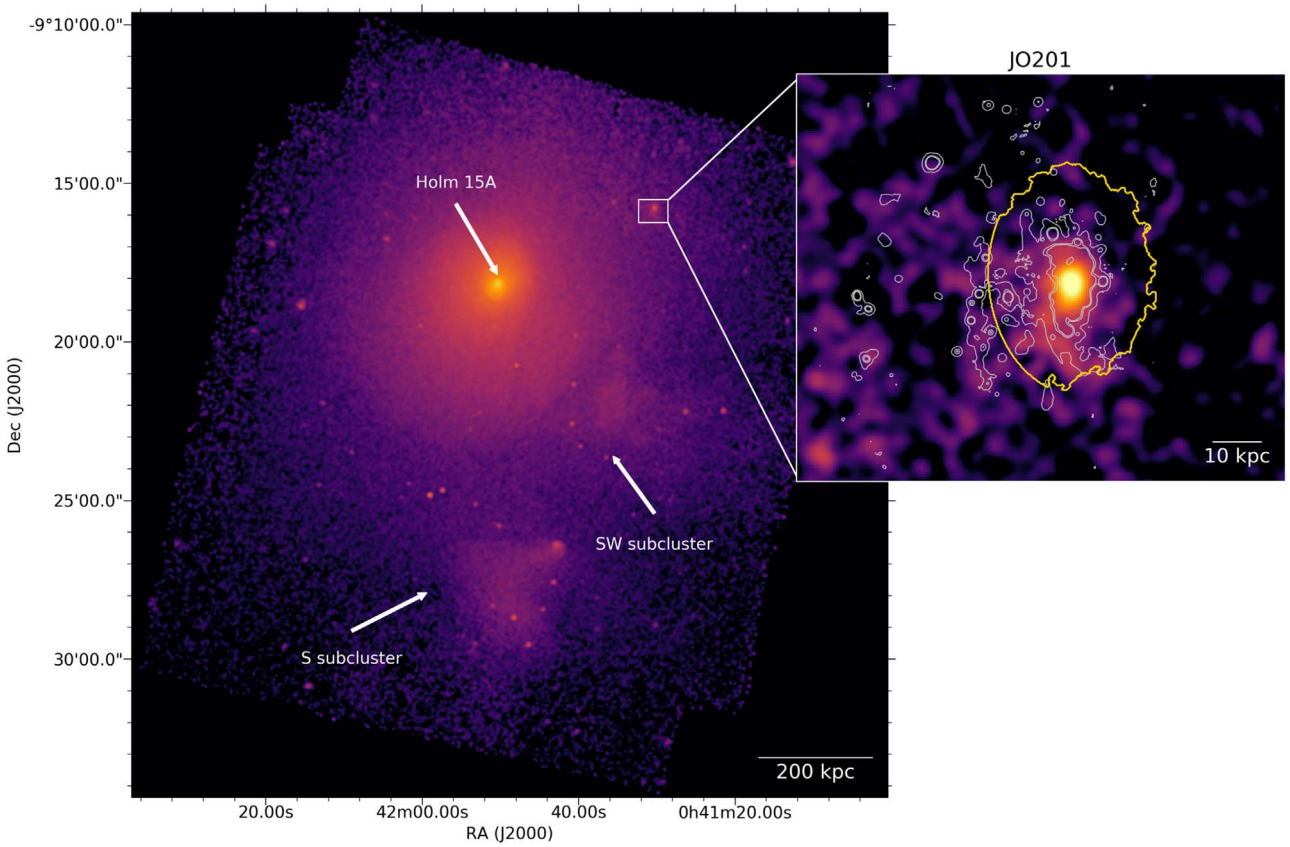

Figure 1. Exposure-corrected mosaic of the cluster A85, Gaussian-smoothed with $\sigma = 2\farcs48$, obtained by combining the five multi-chip Chandra observations and by filtering in the 0.5–2.0 keV band (see Section 3.1 for details). The zoomed-in image shows the galaxy JO201: white contours represent the Hα emission with signal-to-noise ratio (S/N) > 3 (Bellhouse et al. 2019), while the gold contour represents the stellar disk region (Gullieuszik et al. 2020).

field unit (IFU) instrument at the VLT and processed following the standard procedure for GASP galaxies (Poggianti et al. 2017b). The observation was further corrected for extinction by dust within the Milky Way by estimating the contribution using the NASA/IRSA infrared science archive. In order to extract emission line fluxes, the cube was analyzed using the IDL code KUBEVIZ (Fossati et al. 2016) after smoothing spatially with a 5x5 kernel. KUBEVIZ fits a series of Gaussian components to selected emission lines in each spaxel of the IFU data. The resulting map of Hα emission line flux was used in the following analysis.

The maps of emission lines corrected for attenuation were calculated assuming the intrinsic Balmer line ratio of Hα/H$\beta = 2.86$, an ionized gas temperature of $T \approx 10^4$ K , and case B recombination (Osterbrock & Martel 1992). Finally, we discriminated the ionization source of the Hα emission (SF, LINER, or AGN) according to the [O I] diagnostic Baldwin–Phillips–Terchevic (BPT) diagram (Baldwin et al. 1981; Veilleux & Osterbrock 1987). As reported in Poggianti et al. (2019a), at distances of 10–50 kpc from the galaxy center, JO201 shows [O I]/Hα ratios much higher than those observed in SF regions. The other BPT line ratios ([N II]/Hα and [S II]/Hα) are instead closer to values measured in SF regions. Since the LINER-like emission is extended and not concentrated in the nucleus, in this work we refer to these regions as "LIERs" rather than LINERs, following Belfiore et al. (2016).

Unlike the dense ionized gas in H II regions, the DIG component of the ISM has low densities ($n \sim 10^{-1}$ cm^{-3}), high temperatures (higher than $\sim 10^4$ K), and can reach large spatial distances from the H II regions (up to 1–2 kpc; Haffner et al. 2009). The DIG exhibits a lower Hα surface density and higher [S ii]/Hα line ratio compared to the dense gas emission. Fitting the anticorrelation between [S ii]/Hα (accounted for radial gas-phase metallicity gradient) and the extinction-corrected Hα surface brightness, ΣH$\alpha_{\rm corr}$, we derived maps of the fraction of Hα emission due to DIG (labeled hereafter as $C_{\rm DIG}$) through JO201. The details of the DIG fraction estimation are described in Tomičić et al. (2021).

The following point-to-point analysis was carried out with the PT-REX code (Ignesti et al. 2020, Ignesti in preparation) which is based on the Common Astronomy Software Application package[13] (CASA v. 6.0). For sampling the Hα emission, we resort to a grid composed of cells 5″ in size, corresponding to ∼5 kpc. This sampling scale allows us to reconcile the X-ray signal-to-noise ratio (S/N) of each cell (which increases with cell size) with the number of sampled points (which decreases with cell size). The resulting sampling scale is larger than the typical size of SF blobs (∼1–2 kpc) evidenced by the Hα emission in MUSE, and therefore these substructures are subsampled in our analysis. In order to optimize the signal of the galactic emission, we considered only the regions of the Hα image with S/N > 3, and we excluded all those pixels that, according to the BPT diagram, are characterized by the AGN-related emission. Finally, we used the stellar disk mask (Figure 2) to discriminate the cells within the stellar disk (i.e., those that overlap with the stellar

[13] https://casa.nrao.edu/

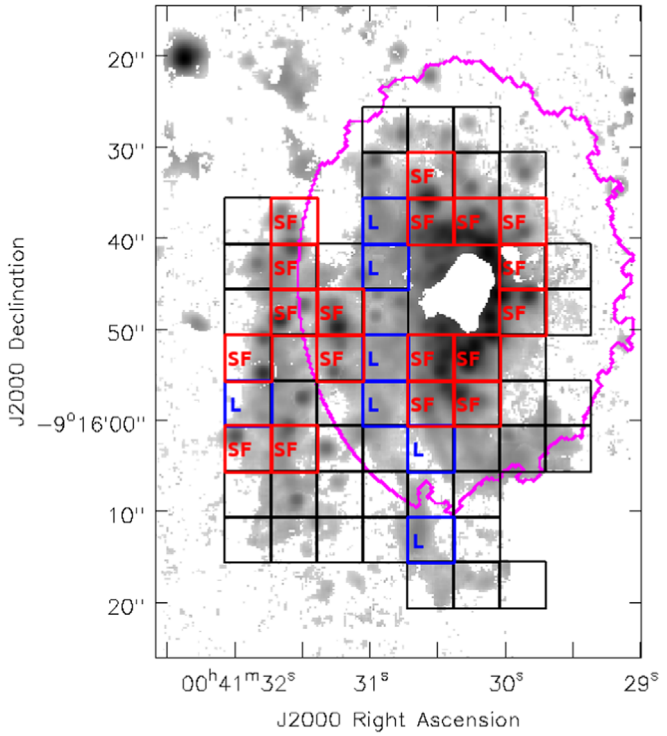

Figure 2. MUSE Hα image with the stellar disk (magenta) and the sampling grid (black) on top, including the SF- and LIER-dominated regions in, respectively, red and blue.

disk mask for >50% of the cell area) from those located over the tail.

We further refined our sampling by identifying those cells with >50% SF-related emission (red) and >50 % LIER-related emission (blue). However, since it was not possible to determine a BPT classification for every spaxel, which is only accepted if all four lines invoked have S/N > 3, we discern the dominant process only in the brightest regions of the galaxy. For this reason, the BPT-spatial correlation analysis does not cover the whole galaxy, but is still able to provide insights of the general trends.

The sampling grid obtained is reported in Figure 2 and is composed of 63 cells, of which 18 were classified as SF-dominated and seven as LIER-dominated. We note that, considering the resolution of the image, the large number of sampling cells assures us that our results are not biased by the choice of the geometry of the sampling grid (we refer the reader to Ignesti et al. 2020, for a more detailed discussion of this issue).

For each cell, we measured both the total Hα surface brightness and the DIG fraction, which we estimated as the total DIG flux density (obtained by multiplying C_{DIG} and Hα in each spaxel) of each cell divided by the Hα flux density, and compared them to the X-ray surface brightness. The correlations were evaluated not only for the whole population, but also for the SF and LIERs regions separately (Figure 4). In particular, using the orthogonal Bivariate Correlated Errors and intrinsic Scatter (BCES) algorithm, which is able to account for the internal scatter of the data (Akritas & Bershady 1996), we fitted the data with a power-law relation $I_{H\alpha}$, DIG fraction $\propto I_X^k$. Finally, in order to estimate the strength of the linear correlations, we computed the Pearson and Spearman correlation ranks (ρ_P and ρ_S), which are reported in the legend of Figure 4, the p-values (p_P and p_S), and the corresponding correlation probabilities ($P_{c,P}$ and $P_{c,S}$). The best-fitting indexes, correlation ranks, p-values, and probabilities are reported in Table 3.

3.4. Spectral Analysis

3.4.1. Spectra Extraction Procedure

The spectral analysis of JO201 was carried out with the software package XSPEC (version 12.10.1f, Arnaud 1996). For each observation, we masked all of the point sources identified by the WAVDETECT in Section 3.1 except the AGN of JO201. In order to study the nature of the interaction between the ICM and the galaxy, we followed the approach proposed in Poggianti et al. (2019b) by considering three regions. The first two relate to the galaxy: one (Figure 6) follows the contours of the Hα emission (Bellhouse et al. 2019) and resembles the X-ray emission; the other one (Figure 3, right panel) traces the contours of the stellar disk and was chosen to compare the SFR estimated from the X-ray luminosity to the SFR obtained in a previous study on the Hα emission in the disk (Vulcani et al. 2018; Gullieuszik et al. 2020). The third region (Figure 3, left panel) was used to determine the properties of the ICM at the same cluster-centric distance of JO201. Under the assumption of the spherical symmetry of the plasma distribution in the northern region of the cluster in which JO201 is moving, we selected an annular region excluding the southwestern part of A85, where the merger with the southern and southwestern subclusters is ongoing (see Section 2.1).

In order to generate the appropriate response matrices, spectra were extracted separately from each observation (or from each chip of each observation in the case of the annular region) and were fitted jointly in the 0.5–7.0 keV band after background subtraction. In the case of the ICM analysis, background spectra were extracted from blanksky files in the same annular region described above. For the galaxy analysis, instead, we tested different extraction procedures, which we summarize in Table 2. On the one hand, we considered two different backgrounds, i.e., case (1) normalized CALDB blanksky files (see Section 3.1), or case (2) local background extracted in an annular region at the same distance and on the same chip of the galaxy. The procedure followed in this latter case allows us to subtract the contribution of the ICM located along the line of sight, which has not been modeled in the fit. On the other hand, we treated the AGN with two different approaches: case (A) including it in the spectrum and modeling in the fit, or case (B) excluding it during the spectrum extraction, by masking an elliptical region of the same size of the Chandra point-spread function at that distance from the pointing center.

3.4.2. Spectral Models

Following the approach presented in Poggianti et al. (2019b), we first investigated the properties of the environment surrounding JO201 to model the contribution of the ICM to the galactic X-ray emission. We fitted the ICM spectra with an absorbed thermal model, tbabs·apec. The tbabs component represents the galactic absorption, and its column density parameter, $n_H = 2.7{\cdot}10^{20}\,cm^{-2}$ was fixed. The apec component instead, describes the emission of a single-temperature plasma, and its temperature, metallicity, and normalization

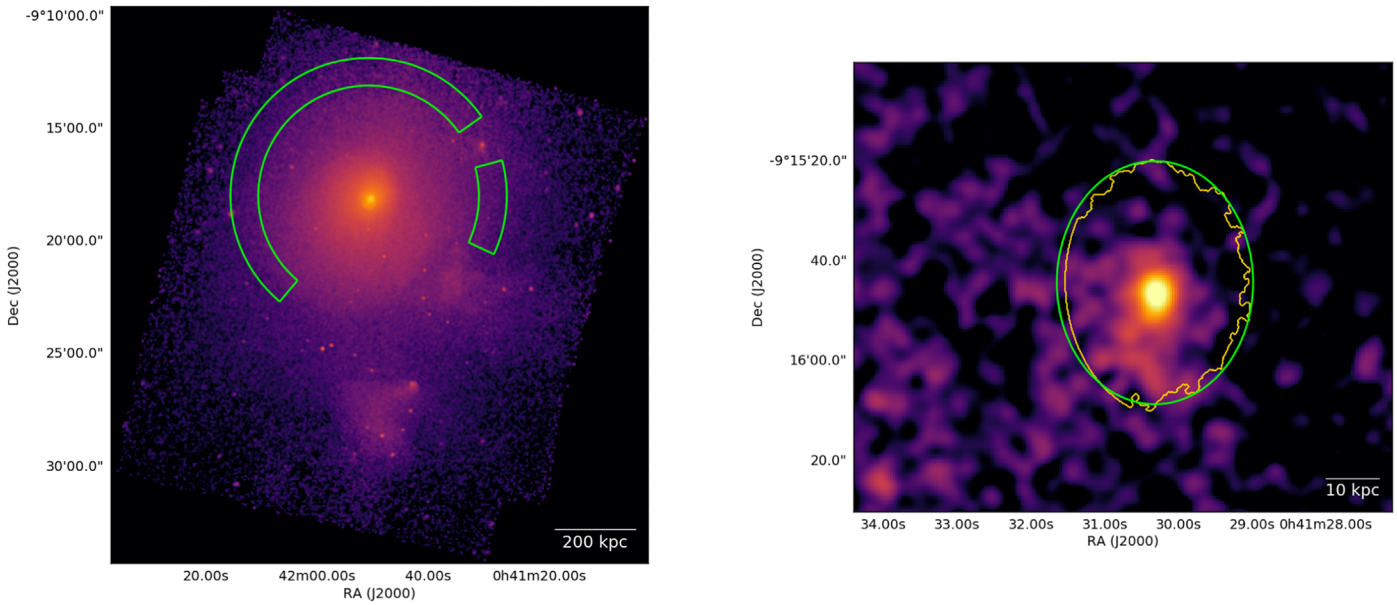

Figure 3. Left panel: exposure-corrected mosaic of the cluster A85 in the 0.5–2.0 keV; the region used for the ICM spectra extraction is shown in green. Right panel: zoomed-in image of JO201; the region used to extract spectra from the stellar disk mask is represented in green, while the contour of the stellar disk (Gullieuszik et al. 2020) used as reference is shown in gold.

Table 2
Configuration Used for the Spectra Extraction and Background/AGN Components Added to the Component That Models the Galactic Emission (i.e., `apec`, `cemekl`, or `mkcflow`).

	AGN Included (Case A)	AGN Excluded (Case B)
`blanksky` (case 1)	`apec+pow`	`apec`
Local background (case 2)	`pow`	...

parameters were let free to vary. The abundance tables used for the entire spectral analysis refer to Asplund et al. (2009).

We then focused on the galaxy to investigate the origin of its extended high-energy emission. In particular, we explore four possible scenarios, which attribute the emission to: (i) the ongoing SF, (ii) the stripping of a galactic hot halo that the galaxy may have possessed, (iii) either the cooling of the ICM onto the galaxy, or the heating of the ISM through shocks and conduction, or (iv) the mixing of the ICM cooling and ISM heating.

To discern which of these hypotheses is correct, we carried out the spectral analysis of JO201. In particular, we tested complex models made of a galactic component chosen among the following:

1. an `apec` model, which describes the emission of a single-temperature plasma and can represent the SF, the hot halo scenarios, and, in a first approximation, the ICM cooling- or the ISM heating-dominated scenarios;
2. a `cemekl` model, describing the emission of a multiphase and multi-temperature plasma where the EM, $\mathrm{EM} = \int n_e n_H dV$, scales with temperature as $EM \propto T^{\alpha}$, and T has an upper limit, T_{MAX}. This model can represent both the hot halo and the ICM–ISM mixing, and from the index α, it is possible to derive the mass-weighted temperature of the plasma as $T_{mw} = T_{\mathrm{MAX}}(1+\alpha)/(2+\alpha)$ (Sun et al. 2010);
3. a `mkcflow` model, which is usually used to describe the thermal cooling of a gas from a maximal, T_{MAX}, to a minimal temperature, T_{min}. This model returns the mass accretion rate parameter ($\dot{M}$) and, in our picture, can represent the ICM cooling scenario (Mushotzky & Szymkowiak 1988).

We include also an additional component that, depending on the extraction procedure used (see Section 3.4.1), models either the ICM along the line of sight or the AGN emission. In particular, we add to the galactic component:

1. an `apec` component when the `blanksky` was used and the AGN was excluded (case 1B). This component takes into account the ICM emission along the line of sight, and its parameters were set to the value determined from the ICM analysis;
2. both an `apec` and a `power-law` component when the `blanksky` was used and the AGN was included (case 1A). We assume in fact that the emission of this central source can be modeled with a power law;
3. a `powerlaw` component to model the emission of the AGN when it was included and the local background was used (case 2A);
4. no component when the AGN was excluded and the local background was used (case 2B).

In each test, we account for the galactic absorption by including a `tbabs` component with a column density of $n_H = 2.7 \cdot 10^{20}\,\mathrm{cm}^{-2}$ (Kalberla et al. 2005). In Table 2 we summarize the four configurations used to extract spectra and the relative components added to the galaxy emission model.

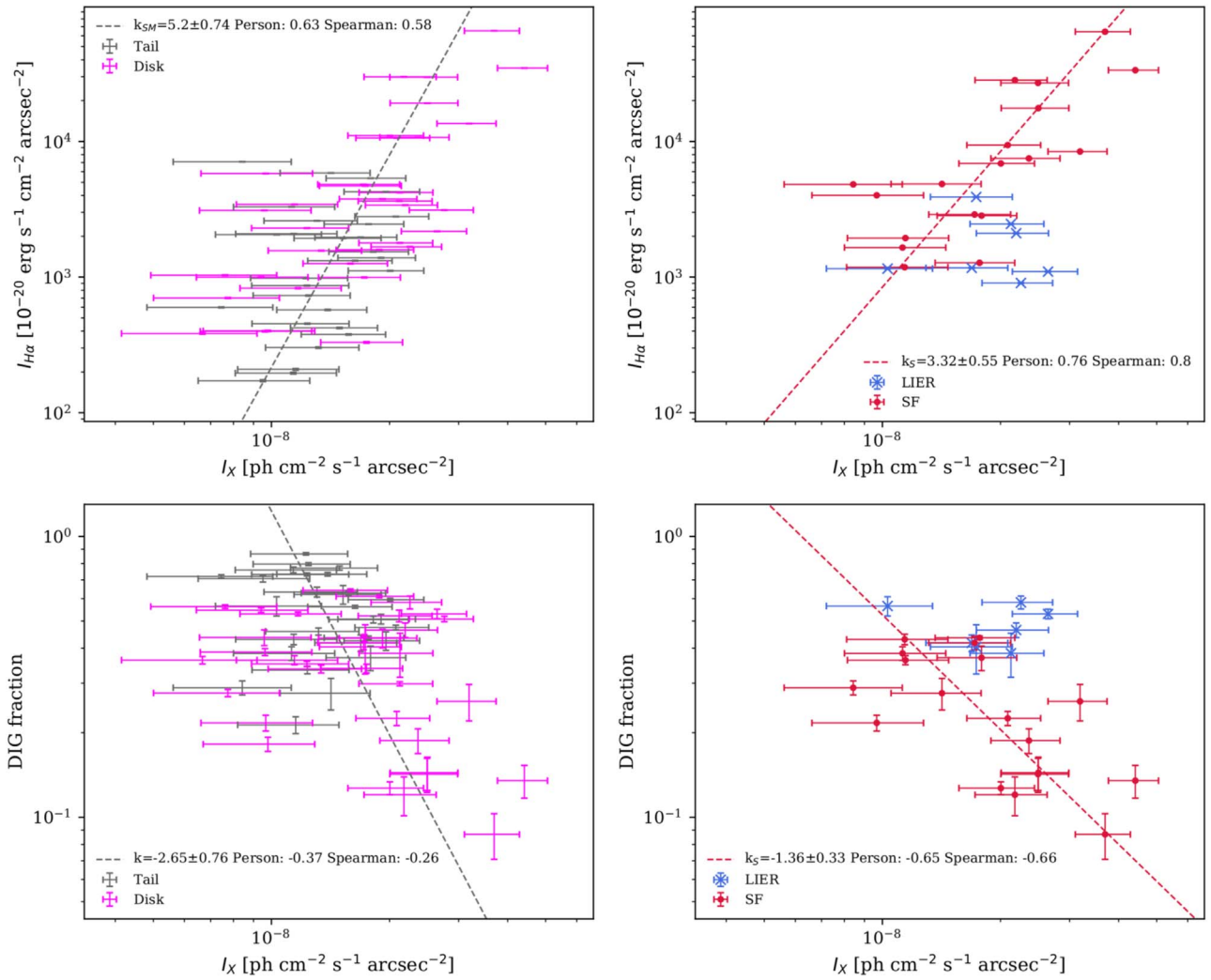

Figure 4. Resulting $I_{H\alpha}$ (top) and DIG fraction (bottom) correlations obtained with the grid presented in Figure 2. In the left panels, we report the distributions obtained by using every cell; cells within the disk are shown in magenta and those in the tail are shown in black. In the right panels, we report the spatial correlations of the SF (red) and LIER (blue) regions. The best-fit indexes are reported in the legends and summarized in Table 3.

4. Results

4.1. Spatial Correlation

In Figure 4 and in Table 3 we report the results of the point-to-point analysis carried out with the grid presented in Figure 2. The majority of regions are characterized by lower Hα and X-ray surface brightness and higher DIG fraction, whereas the brightest spots, which are located in the innermost part of the disk, show a lower DIG fraction. The BPT-based sampling highlights that the SF-dominated regions have, generally, a higher $I_{H\alpha}$ and lower DIG fraction with respect to the LIER-dominated regions.

We observe a positive correlation between Hα and X-ray surface brightness (Figure 4, top-left panel), and a putative anticorrelation between DIG fraction and X-ray surface brightness (Figure 4, bottom-left panel). The two correlations became more evident when we limited our analysis to the SF-dominated regions. On the contrary, LIER-dominated regions did not show any evident correlation (Figure 4, right panels).

4.2. Results of the Spectral Analysis

In this subsection we report the results obtained by the spectral analysis of both the AGN and the galactic emission.

4.2.1. AGN

The central source in JO201 has a shape consistent with a point source at a distance of $\sim 5'$ from the aimpoint. We extract the spectrum from a circular region of $4''$ enclosing the central source, and we use the surrounding annulus as a background that includes the underlying cluster (A85) background, the instrumental background, and the galaxy diffuse background. The resulting number of net counts is not enough to allow for a thorough spectral analysis: with around 100 net counts, the extracted spectrum is well fitted by a power law, absorbed by the Galactic n_H. However, the resulting slope, $\Gamma = 2.7 \pm 0.2$, is steeper than usual in AGNs. A more complex model is therefore adjusted to the data: a `pexrav` with the addition of a Gaussian line. The model describes the reflection spectrum off the walls of the torus surrounding the AGN. The match is good with an intrinsic "canonical" $\Gamma = 1.7$ and a high degree of reflection, as in a Compton-thick AGN. The energy of the Gaussian line is consistent with a 6.4 keV KαFe emission

Table 3
Results of the Point-to-point Analysis Presented in Figure 4

	k	ρ_P	p_P	$P_{c,P}$	ρ_S	p_S	$P_{c,S}$
			$I_{H\alpha}$ vs. I_X				
Total	5.17 ± 0.73	0.63	3.32×10^{-8}	0.99	0.58	7.99×10^{-7}	0.99
SF	3.32 ± 0.55	0.76	2.86×10^{-4}	0.99	0.80	5.82×10^{-5}	0.99
LIER	none	0.02	0.96	0.04	−0.39	0.38	0.62
			DIG fraction vs. I_X				
Total	-2.58 ± 0.74	−0.37	2.86×10^{-3}	0.99	−0.26	3.95×10^{-2}	0.96
SF	-1.29 ± 0.30	−0.65	3.25×10^{-3}	0.99	−0.66	3.16×10^{-3}	0.99
LIER	none	−0.14	0.82	0.18	0.25	0.59	0.41

Note. From left to right: sampled points; index of the best-fit power law; Pearson rank; Pearson p-value; Pearson correlation probability; Spearman rank; Spearman p-value; Spearman correlation probability.

redshifted at the $z = 0.055$ of the galaxy. The resulting luminosity is $L_X^{0.5-10\,\mathrm{keV}} = 2.7 \times 10^{41}$ erg s^{-1}. [14] However, the intrinsic luminosity could be at least a factor of 100 higher, given the torus absorption. This is also in accordance with the optical classification of the source as Type 2 (Radovich et al. 2019). A higher statistics, or observations at higher energies, would be needed to derive precise parameters for the source.

4.2.2. Galaxy

Our spectral analysis of the X-ray emission associated with JO201 did not reveal significant discrepancies between the four procedures tested for the spectra extraction (see Section 3.4.1). In this section we report the tests performed with the configuration that requires the simplest model and ensures the higher number of counts, i.e., 1B (`blanksky` and AGN subtraction). The spectral results obtained with the Hα and the stellar disk mask are consistent in terms of both the best-fit parameters and the χ^2 values. For this reason, aiming to realize a comparison between the SFR estimated from the X-ray luminosity and the SFR found in Vulcani et al. (2018) from the Hα emission in the disk, we choose to present the results obtained with the stellar disk mask, whereas those obtained with the Hα mask are presented in the Appendix.

Following the approach described in Section 4, we first estimated the properties of the surrounding ICM. In agreement with the previous results of Ichinohe et al. (2015; see Section 2.1), we found a temperature of $kT = 7.1 \pm 0.2$ keV and a metallicity of $Z = 0.21 \pm 0.04\ Z_\odot$. Based on the temperature, we estimated a local speed of sound $c_s \simeq 520\sqrt{kT/(1\,\mathrm{keV})} \simeq 1376$ km s^{-1}, which entails a galactic Mach number $\mathcal{M} \simeq 2.4$.

We then carried out the modeling of the X-ray emission from the region of the stellar disk, following the procedure described in Section 3.4.2. In particular, we built our model by adding to the galactic component (`apec`, `cemekl`, or `mkcflow`) an `apec` component that takes into account the ICM emission along the line of sight (1B configuration in Table 2); we report the results of the fits in Table 4.

Our criterion to attest the validity of a model was based not only on the values of the χ^2 obtained, but also on the values of the temperature, T, and metallicity, Z, revealed by the fits. Thus, we have found a temperature of $kT = 0.79^{+0.08}_{-0.08}$ keV for model (1) `apec+apec`, $kT_{MAX} = 1.2^{+0.4}_{-0.2}$ keV for model (3) `apec+mkcflow`, and $kT_{MAX} = 1.1^{+0.5}_{-0.2}$ keV for model (4) `apec+mkcflow`. In all three cases, the values obtained are lower than the ICM temperature, a sign that the emitting plasma is in an intermediate phase between that of the ICM and that of the ISM. For model (2) `apec+cemekl`, instead, we noticed that by leaving the temperature parameter free to vary, it was not possible to obtain a good fit of the data. Since the `cemekl` model describes the emission of a multiphase and multi-temperature plasma, we supposed that the maximal value that the temperature can assume is the value of the ICM temperature, and for this reason, we fixed $T_{MAX} = 7.1$ keV. The best-fit $\alpha = 0.01^{+0.10}_{-0.01}$ would entail a $T_{mw} \simeq 3.5$ keV and an almost uniform emission measure (EM) of the plasma.

Regarding metallicity, we note that, when it was set free (models (1) and (4)), the Z values obtained were lower than those of the ICM. We considered these values implausible, because the X-ray emitting plasma is either the ICM, or the ISM, or a mixture of these two components, and thus its metallicity is expected to vary between the values of the ICM metallicity ($Z_{ICM} = 0.21\ Z_\odot$, see Section 3.4.2) and those of the ISM metallicity (typical values are $Z \sim 1\ Z_\odot$). In the other two cases (models (2) and (3)), it was not possible to obtain a good fit of the data by letting this parameter free. For this reason, we fixed it to the value of the ICM.

Under a statistical point of view, the four models are indistinguishable because they fit the observations equally well, as it is possible to notice from the values of the χ^2_R.

5. Discussion

5.1. Origin of the X-Ray Emission

The correlation between X-ray and Hα surface brightness (Figure 4, top panels) indicates that the galactic X-ray emitting medium closely follows the spatial distribution of the ISM. This result suggests that the X-ray emission arises from local, small-scale processes taking place in close proximity of the ISM. A similar behavior was also observed both in the disk of isolated galaxies (Ranalli et al. 2003; Symeonidis et al. 2011; Mineo et al. 2014) and on jellyfish galaxies in Sun et al. (2010) and Poggianti et al. (2019b). In the first case, given the lack of a hot surrounding ICM, the correlation was interpreted as a consequence of recent star-forming processes. In the second case, since JW100 and ESO 137-001 are located in a cluster environment and show an X-ray luminosity higher than expected from SF, it was suggested that the high-energy

[14] We note that this is lower than reported in Poggianti et al. (2017a; $L_X^{0.3-8\,\mathrm{keV}} = 7.3 \times 10^{41}$ erg s^{-1}) due to the different spectral model we adopted.

Table 4
Fit Results for Spectra Extracted from the ICM Region ("Control Region", Figure 1) and from the Stellar Disk Mask ("JO201", Figure 3, Right Panel)

	Model	Parameters	χ^2/dof χ^2_R
Control region (ICM)	(0)tbabs·apec	$kT = 7.1 \pm 0.2$, $Z = 0.21 \pm 0.04$	1694.7/1617
		$F = (8.65 \pm 0.17) \cdot 10^{-13}$, $L = (2.73 \pm 0.08) \cdot 10^{42}$	1.048
JO201	(1) tbabs·(apec+apec)	$kT = 0.79\ ^{+0.08}_{-0.08}$, $Z = 0.08^{+0.08}_{-0.04}$	43.18/47
		$F = (4.1 \pm 0.5) \cdot 10^{-14}$, $L = (1.9 \pm 0.3) \cdot 10^{41}$	0.9187
	(2) tbabs·(apec+cemekl)	$\alpha = 0.01^{+0.10}_{-0.01}$	40.76/48
	$Z = 0.21$ and	$F = (9.4 \pm 0.8) \cdot 10^{-14}$, $L = (4.5 \pm 0.4) \cdot 10^{41}$	0.8492
	$kT_{MAX} = 7.1$ keV (fixed)		
	(3) tbabs·(apec+mkcflow)	$kT_{min} = 0.08^{+0.27}_{-0.08}$, $kT_{MAX} = 1.2^{+0.4}_{-0.2}$	
	40.07/47		
	$Z = 0.21$ (fixed)	$\dot{M} = 1.7^{+0.4}_{-0.6}$	0.8526
		$F = (4.4 \pm 0.6) \cdot 10^{-14}$, $L = (1.9 \pm 0.3) \cdot 10^{41}$	
	(4) tbabs·(apec+mkcflow)	$kT_{min} = 0.08^{+0.35}_{-0.08}$, $kT_{MAX} = 1.1^{+0.5}_{-0.2}$	39.78/46
		$\dot{M} = 2.1^{+3.5}_{-1.1}$. $Z = 0.13^{+0.27}_{-0.09}$	0.8609
		$F = (4.3 \pm 0.5) \cdot 10^{-14}$, $L = (3.3 \pm 0.4) \cdot 10^{41}$	

Note. For the latter region, we resort to the 1B extraction configuration, which models the ICM emission with an additional apec component (see Section 3.4.2). The best-fit parameters shown in the third column refer only to the galactic component indicated in the second column (namely, (1) apec, (2) cemekl, and (3) and (4) mkcflow). The unit measures used are: keV for temperature (kT), $Z_\odot$ for metallicity (Z), $M_\odot$ yr^{-1} for the mass accretion rate ($\dot{M}$), erg s^{-1} cm^{-2} for flux (F), and erg s^{-1} for luminosity (L). The unabsorbed flux and luminosity refer only to the galactic component and were measured in the 0.5–10.0 keV energy band.

emission arises from the local interplay between the ICM and the ISM and that it could be produced by the interface between the ICM and the ISM.

Starting from these two different scenarios, we investigated the contribution of the SF to the X-ray luminosity of JO201, following the approach presented in Poggianti et al. (2019b). In the presence of SF, the X-ray luminosity of a galaxy is indeed usually dominated by the contribution of both high-mass X-ray binaries, whose characteristic lifetime is 10^7 yr, and hot ISM, which is ionized by supernovae and massive stars (e.g., Mineo et al. 2014). Since the sum of these contributions correlates with other SFR indicators, many relations have been developed to link the L_X of a galaxy to its SFR (and vice versa).

Using the L_X-SFR calibration of Mineo et al. (2014) converted from a Salpeter to a Chabrier IMF and from 0.5–8 keV to 0.5–10 keV assuming a factor 1.11,

$$L_{X,0.5-10.0\,\mathrm{keV}} = 7.6 \cdot 10^{39}\,\mathrm{SFR\ \ erg\ s^{-1}} \quad (1)$$

where the SFR is in units of $M_\odot$ yr^{-1}, we estimated an $L_X \sim 3.8 \cdot 10^{40}$ erg s^{-1}, which is lower by one order of magnitude than the values found by our models (see Table 4).

From this result, we conclude that SF alone is not able to produce the observed X-ray luminosity and that an additional contribution is necessary, likely coming from the ongoing stripping process. This discrepancy between predicted and observed X-ray luminosity has been observed also for JW100 (by a factor of 4–10; Poggianti et al. 2019b); thus, we suggest that it could be a common feature among jellyfish galaxies with extended X-ray emission. Further studies in this direction are now necessary to test our speculations.

The point-to-point analysis also revealed that the SF regions are generally above the LIERs ones in the Hα-X plot (Figure 4). An alternative view on these results is that, for similar values of $I_{H\alpha}$ or the DIG fraction, the LIER regions show higher values of I_X than do the SF regions. This latter feature is similar to what was previously observed in JW100 (Poggianti et al. 2019b). We also note that the main correlations are driven by the SF-dominated regions, whereas the LIER regions, which are present only in the low Hα brightness or high-DIG fraction degree part of the plots, are less correlated.

Concerning the connection between DIG fraction and X-ray emission, we observe that LIER regions, which are located mostly along the stripped arm (Figure 2), show a generally higher DIG fraction. This behavior suggests that the DIG regions in the stripped tail may present more LIER features compared to the dense gas in the stellar disk, which is SF-dominated. Finally, the putative anticorrelation between the DIG fraction and I_X could be explained by the fact that the DIG-dominated regions typically have lower Hα flux compared to the dense gas-dominated regions (e.g., Madsen et al. 2006; Haffner et al. 2009; Tomičić et al. 2021). Thus, following the $I_{H\alpha} - I_X$ correlation, the DIG-dominated regions would show lower X-ray emission compared to the dense gas-dominated regions.

Having established that SF alone is not able to generate the X-ray emission of JO201, we are left with the other three scenarios presented in Section 3.4.2, i.e., stripping of the galactic hot halo, cooling of the ICM onto the galaxy or heating of the ISM through shocks and conduction, and mixing of the ICM cooling and ISM heating. The stripping of the hot galactic halo that JO201 may have possessed could produce extra-planar X-ray emission. However, the face-on orientation of the galaxy makes it difficult to verify this scenario. Nevertheless, many studies (e.g., Larson et al. 1980; Bekki et al. 2002; Zinger et al. 2018; Jaffé et al. 2018; Poggianti et al. 2019b; Gullieuszik et al. 2020) highlighted the fact that the majority of galaxies lose their halo in their fall toward the cluster center, before reaching the virial radius. Given the proximity of JO201 to the cluster center, well inside the virial radius, we considered that the loss of its halo has already occurred and thus that this scenario is implausible. Therefore, the remaining scenarios are the heating of the ISM (through shocks, conduction, or turbulent mixing resulting from the interaction with the ICM), and the cooling of the ICM onto the galaxy (again through conduction or mixing or a combination of the two scenarios). From our spectral analysis, we found that the models tested lead to statistically equivalent results (see

Section 4.2.2), and for this reason, we are not able to discern which of these hypotheses is superior. Nevertheless, in the following section, we sift through each scenario, trying to deepen our knowledge about their physics and their implications.

5.2. Insights from the X-Ray Spectral Models

In order to gain further insights from the X-ray spectral analysis of JO201, we explored the results obtained from the different spectral models in greater depth. As a first step, we considered the model (1) tbabs·(apec+apec) to estimate the mass of the hot galactic plasma. As explained in Section 3.4.2, the first apec represents the ICM emission along the line of sight. For this reason, we can assume that the best-fit values reported in Table 4 and related to the galactic component (namely to the second apec) are de-projected quantities. Starting from this consideration, the normalization of the apec model is linked to the volume of the X-ray emitting plasma through the relation:

$$V = \frac{4\pi N [D_A(1+z)]^2}{n_e n_p 10^{-14}} \quad (2)$$

where N is the normalization parameter of the apec model, z is the redshift, $D_A = 5.26{\cdot}10^{26}$cm is the angular distance, and n_p is the proton number density, ($n_p = 0.8\ n_e$; e.g., Gitti et al. 2012). We then followed two parallel procedures. In the first case, we started from the assumption of pressure equilibrium between the ICM ($n_e \sim 10^{-3}\,\mathrm{cm}^{-3}$ and $kT = 7.1 \pm 0.2$ keV) and the galactic hot ($kT \sim 1$ keV) plasma, finding that this latter component is characterized by an electron density of $n_e = (6.4 \pm 0.2){\cdot}10^{-3}\,\mathrm{cm}^{-3}$. Using the relation from Equation (2), we deduced that this plasma is included in a volume, $V = (1.8 \pm 0.3) \cdot 10^{69}\,\mathrm{cm}^3$, and consequently its mass is

$$M_{gas} = \rho_{gas} V = 1.9 n_e m_p \mu V = (1.1 \pm 0.2) \cdot 10^{10} M_\odot \quad (3)$$

where ρ_{gas} is the mass density of the emitting gas, $\mu = 0.6$ is the mean molecular weight, and m_p is the proton mass.

The second procedure that is adopted to estimate the mass assumes that the hot galactic plasma occupies a cylindrical volume, with a height equal to the length of the gaseous tail (94 kpc; Bellhouse et al. 2019) and an elliptical basis with the same dimensions of the stellar disk (semiminor axis, $b_{min} = 10.7 \pm 0.5$ kpc, and semimajor axis, $b_{max} = 13.3 \pm 0.5$ kpc; Gullieuszik et al. 2020), uniformly filled by the hot plasma (i.e., with a filling factor $\phi = 1$). As a result of these assumptions, we consider our estimates to be an upper limit of the real volume of the tail. We then estimate the n_e parameter by inverting Equation (2). Also in this case, we can assume that the normalization of the apec component associated with the galactic emission is a de-projected quantity, because we are modeling the contribution of the ICM along the line of sight with an additional apec component (see Section 3.4.2). The electron number density measured in this case is $n_e = (8.0 \pm 0.5) \cdot 10^{-3}\,\mathrm{cm}^{-3}$, and consequently, using Equation (3), the mass of the X-ray emitting gas is $M_{gas} = (9.2 \pm 1.5) \cdot 10^9\ M_\odot$. We note that our estimates are close to the predicted mass of the gas with temperature $7 \times 10^5\,\mathrm{K} < T < 7 \times 10^7\,\mathrm{K}$ reported by Tonnesen et al. (2011) for a high-velocity jellyfish galaxy ($9.1 \times 10^9\ M_\odot$).

The second model studied in detail is the tbabs·(apec +mkcflow), which describes the ICM cooling scenario. As reported in section Section 2.2, JO201 shows in fact a high fraction of molecular gas and a high SFR, which suggest the presence of an additional source of cold gas in the galaxy. For this reason, we took into consideration the hypothesis that the dominant process responsible for the extended X-ray emission could be the cooling of the ICM onto the galaxy. In this scenario, the increase of the fraction of molecular gas and the corresponding enhancement of the SFR would be fueled by the continuous accretion of cooling ICM onto the galaxy. In this treatment, we refer to model (3)—see Table 4—where the metallicity of the mkcflow component is fixed to $Z = 0.21\ Z_\odot$.[15] The spectral analysis determined a cooling rate of $\dot{M} = 1.7^{+0.4}_{-0.6}\ M_\odot\ \mathrm{yr}^{-1}$, which is close to the observed excess of SFR, $\sim 3\ M_\odot\ \mathrm{yr}^{-1}$, with respect to the median SFR expected for a galaxy of similar mass (Vulcani et al. 2018). This supports the idea that the SFR could be actively fueled by the cooling gas.

Finally, in order to constrain the limits of this pure radiative cooling scenario, we estimated the cooling time of the X-ray emitting plasma with the relation (e.g., Gitti et al. 2012):

$$t_{cool} = \frac{5}{2} \frac{kT}{\mu X_H n_e \Lambda(T)} \quad (4)$$

where $X_H = 0.71$ is the hydrogen mass function, and Λ(T) is the cooling function (we have interpolated the table by Sutherland & Dopita 1993 as a function of temperature and metallicity). By adopting the values of the galactic hot plasma ($n_e = 6.4 \pm 0.2 \times 10^{-3}\,\mathrm{cm}^{-3}$ and $kT \sim 1$ keV), the resulting timescale is $t_{cool} \approx 3.6$ Gyr, which is not consistent with the time in which the galaxy has experienced the stripping process (0.6–1.2 Gyr; see Section 2.2). This tension could be relieved if the galactic hot plasma had a filamentary structure composed of several clumps with a higher local density (i.e., a volume with $\phi \ll 1$), which would produce a patchy thermal emission with local peaks where, due to the higher X-ray emissivity, the ICM would cool down faster. On the other hand, the discrepancy between the average cooling time estimated above and the stripping time demonstrates that the cooling process could be not only radiative, but it could occur also through conduction or mixing with the ISM (e.g., Fielding et al. 2020).

5.3. Origin of [O I]/Hα Excess

A number of jellyfish galaxies show an excess of [O I]/Hα emission in their tails, whose origin is unclear (Fossati et al. 2016; Poggianti et al. 2019b, 2019a). On the basis of our results and those presented in Poggianti et al. (2019b), we speculate that it might be related to the presence of a warm plasma surrounding the stripping filaments (see Section 4.2.2). To test this hypothesis, we used the CLOUDY C17.02 (Ferland et al. 2017) photoionization code to predict the emission line ratios produced by a cold ISM cloud embedded in a warm plasma, whose properties are constrained by our results (Section 4). To this end, we first derived with CLOUDY the continuum emitted by a warm plasma described as a collisionally ionized gas with $kT \simeq 1$ keV and a hydrogen density $n_H \sim 10^{-2}\,\mathrm{cm}^{-3}$. We then

[15] By using model (4), where the metallicity was let free to vary, both a value of metallicity lower than that of the ICM and a higher error for the mass accretion rate, $\dot{M}$, were measured.

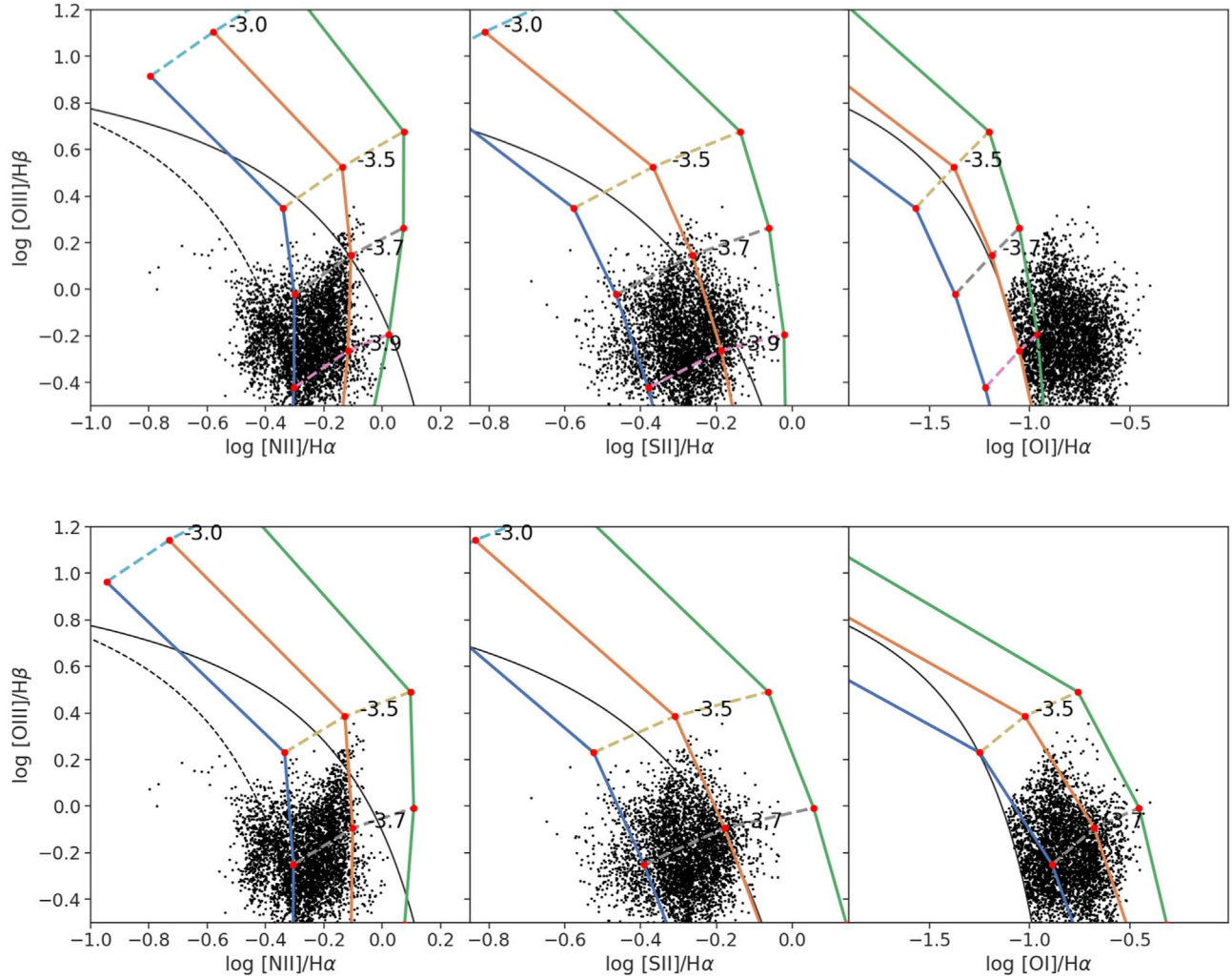

Figure 5. Comparison of line ratios in spaxels classified as LIERs (black dots, distributed as shown in Figure 2) and CLOUDY photoionization models with different metallicities (from left to right: $Z/Z_{\odot} = 0.3$, 0.5, 1) and ionization parameters ($-4 \leqslant \log U \leqslant -3$), and $n_{\rm H} = 10$ cm^{-3}. The upper and lower panels show the results obtained with column densities $\log N_{\rm H} = 17$, 19.5, respectively. The black solid and dotted curves display the SF/LIER classification by Kewley et al. (2006).

computed a grid of models for clouds ionized by this continuum, varying the ionization parameter (U), hydrogen density ($n_{\rm H}$), column density ($N_{\rm H}$), and metallicities (Z). The ionization parameter is defined as the ratio of the surface flux of ionizing photons to the hydrogen density, $U = \Phi(H)/(n_{\rm H}c)$ (Osterbrock & Ferland 2006). We then looked for the models that provide the best fit to the line ratios measured in the spaxels classified as LIERs.

A good agreement is obtained with the following parameters: $n_{\rm H} \leqslant 10$ cm^{-3}, $\log U \leqslant -3.5$, $Z/Z_{\odot} \sim 0.3$–0.5, and $\log N_{\rm H} \sim 19.5$. The constraint on the column density is given by the relatively high [O I]/Hα ($\sim$0.1), which requires that the clouds must be ionization bounded. The BPT diagram is displayed in Figure 5 and compares the observed line ratios with those produced by photoionization models in a region around the best-fit parameters.

We conclude that the ionization triggered by the warm plasma would be able to reproduce the [O I]/Ha excess in the LIER regions, or at least significantly contribute to it. A similar excess in [O I]/Ha was also found in the stripped gas component of ESO 137-001 (Fossati et al. 2016) and UGC 6697 (Consolandi et al. 2017), who interpreted it to the presence of shocks. A more detailed analysis, including data from more jellyfish galaxies, will be the subject of a separate paper.

5.4. Comparison with Previous Works

Finally, we compare the results of our work with previous studies of the galaxies NGC 4569 (Tschöke et al. 2001), NGC 6872 (Machacek et al. 2005), UGC 6697 (Sun & Vikhlinin 2005; Consolandi et al. 2017), ESO 137-001 and ESO110137-002 (Sun et al. 2010; Zhang et al. 2013), and JW100 (Poggianti et al. 2019b). Despite the differences between these galaxies, in terms of stellar mass and velocity, and the properties of the respective environments, the X-ray analysis revealed a number of similarities that can help outline the origin of the X-ray emitting plasma. Here we list the common aspects:

1. The X-ray temperature derived for these galaxies with the single-temperature model, i.e., the average spectral temperature, is in between 0.7 and 1.0 keV. This value is not consistent with neither the typical temperature of hot gas in normal spirals ($kT \sim 0.3$ keV; e.g., Strickland et al. 2004; Mineo et al. 2012), nor with the temperature of the surrounding environment;

2. The galaxies for which it was possible to reliably estimate the velocity show similar Mach numbers $\mathcal{M} = 2$–2.5;
3. For the only exception of NGC6872 that is part of a galaxy group, the ICM thermal pressure surrounding these galaxies ranges between 0.8 and 4.2×10^{-11} erg cm^{-3}. These values are consistent with threshold of $\sim 0.9 \times 10^{-11}$ erg cm^{-3} defined in Tonnesen et al. (2011) for the formation of bright Hα and X-ray filaments.

For JW100 and JO201, we identify additional similarities based on the MUSE analysis:

1. These galaxies show an excess of [O I]/Hα emission along their tails, in correspondence of LIER/composite regions. For JW100, the LIER emission represents the majority of the Hα emission outside of the stellar disk, whereas in JO201, we observe a lower fraction of LIER emission, but we cannot exclude the role of projection effects in this;
2. We observe in these galaxies a positive spatial correlation between Hα and X-ray surface brightness, which suggests that in both galaxies, the X-ray emitting plasma follows closely the distribution of the stripped ISM (or vice versa);
3. Despite the different sampling techniques, we observe a similar behavior between star-forming and LIER regions, where the former are generally located to the top-left part of the $I_{\mathrm{H}\alpha} - I_{\mathrm{X}}$ plane with respect to the latter (Figure 4). This could be interpreted either as an excess of Hα emission of the star-forming region with respect to the LIER regions, or as an excess of X-ray emission of the LIER regions with respect to the star-forming blobs. However, we note that contrary to Poggianti et al. (2019b), the LIER emission does not seem to correlate with the X-ray. This difference could be due to projection effects, where the orientation of the tail of the galaxy with respect to the line of sight reduces the number of sampling cells at our disposal and strongly affects our results.

This comparison illustrates a scenario where the X-ray emission arises from the interplay between the ISM and the ICM over the stripped tails (as highlighted by the spatial correlation), which is driven by the galactic Mach number and the environmental pressure. This physical framework resembles that of a cold cloud embedded in an hot wind, which has been deeply explored in the literature by means of numerical simulations (e.g., Vollmer et al. 2001; Tonnesen et al. 2011; Scannapieco & Brüggen 2015; Sparre et al. 2020; Kanjilal et al. 2021). Albeit all of the works predict that the ICM–ISM interplay would lead to the origin of a warm "mixing layer" between the two, their properties and fate are still debated. Therefore, we suggest that the X-ray emitting plasma we studied could correspond to the high-temperature component of the "mixing layer" predicted by the simulations. Furthermore, we argue that the emergence of the [O I]/Hα excess in the stripped tails could be another consequence of this ICM–ISM interplay, as consequence of the ionization of the ISM due to the proximity of a warm plasma.

The study of the polarized radio emission of jellyfish galaxies can provide complementary insights into this scenario. Müller et al. (2021) discovered that the magnetic field of another jellyfish galaxy of the GASP sample, JO206, is remarkably ordered along the stripped tail. They suggest that this is consequence of the draped accretion of the ICM onto the galaxy during its motion, which produces a magnetized "draping sheath" lit up by the cosmic rays (Sparre et al. 2020). Transposed to our findings, this ICM draping process could play a role in the origin of the X-ray emitting plasma by favoring ICM accretion onto the stripped tails of jellyfish galaxies. Exploring this scenario in detail requires similar radio studies for JO201 and/or deep X-ray observations of JO206.

6. Summary and Conclusions

In this paper we have investigated the thermal side of one of the most extreme objects of the GASP sample: JO201. This jellyfish galaxy is experiencing a strong stripping process triggered by the ICM of its host cluster A85 and shows extended X-ray emission. We carried out the first detailed investigation of the X-ray emission of JO201 by means of both a spectral analysis and a point-to point spatial correlation between the Hα and the X-ray emission. The data set used was composed of five Chandra archival observations (total exposure time $t_{exp} \sim 187$ ks), MUSE Hα cubes, and an emission fraction of the DIG maps.

We found that the X-ray luminosity of the galaxy is provided by two contributions. The first one is related to the AGN ($L_X^{0.5-10\,\mathrm{keV}} = 2.7 \cdot 10^{41}$ erg s^{-1}, not corrected for intrinsic absorption), whose emission describes the reflection spectrum of the walls of the torus surrounding the black hole. We reveal an intrinsic photon index of $\Gamma = 1.7$ and a high degree of reflection, as expected in a Compton-thick AGN. The second contribution is provided by an extended source associated with a warm plasma ($kT \approx 1$ keV) whose X-ray luminosity $L_X^{0.5-10\,\mathrm{keV}} \approx 1.9$–$4.5 \cdot 10^{41}$ erg s^{-1} is one order of magnitude higher than the X-ray luminosity expected from the only SF ($L_X^{0.5-10.0\,\mathrm{keV}} \sim 3.8 \cdot 10^{40}$ erg s^{-1}). The correlation between the Hα and X-ray surface brightness emerging from the point-to-point analysis reveals that this galactic X-ray emitting plasma closely follows the spatial distribution of the ISM. These behaviors suggest that the X-ray extended emission associated with the galaxy results from the local interplay between the ICM and the ISM, but it also could be produced by the interface between the two components that envelopes the stripped ISM.

In order to investigate the nature of this interplay, we tested three different spectral models. However, since they all provide statistically consistent results, we were not able to discern if the X-ray emission is caused by the heating of the ISM, the cooling of the ICM onto the galaxy, or the mixing of the ISM and ICM through shocks and conduction. We have therefore deepened our study by taking into consideration the following peculiar properties of JO201 emerging from previous studies: the galaxy shows a high fraction of molecular gas (four to five times higher than that observed in galaxies of the same mass) and an SFR 0.4–0.5 dex above the main sequence of non-stripped disk galaxies. Furthermore, it is characterized by an excess of [O I]/Hα emission in correspondence of its tail.

Starting from the high fraction of molecular gas and the high SFR, we suggest the presence of an additional source of cold gas, which could arise from the cooling of the ICM onto the galaxy. We thus compare the cooling rate obtained from the spectral analysis ($\dot{M} = 1.7^{+0.4}_{-0.6}\ M_\odot$ yr^{-1}) to the excess of SFR ($\sim 3\,M_\odot$ yr^{-1}), finding that the two values are very close. However, the cooling time of the X-ray emitting plasma, $t_{\mathrm{cool}} \approx 3.6$ Gyr, is higher than the stripping time,

$t_{\rm stripping} = 1.2$–0.6 Gyr. On the one hand, this discrepancy could be the result of a filamentary structure composed of several clumps with a higher local density where, due to the higher X-ray emissivity, the ICM cools down faster. On the other hand, the high cooling time could indicate that the cooling process is not only radiative, but occurs also through conduction or mixing with the ISM.

In this work we also investigated the origin of the [O I]/Hα excess observed in JO201, as well as in other jellyfish galaxies. Specifically, we tested the possibility that this emission could originate from the presence of the warm plasma surrounding the stripped ISM. For this reason, we simulated with CLOUDY the behavior of a cold cloud embedded in a warm plasma, whose thermal properties were constrained by the spectral analysis. From the comparison between the results of the simulations and the line rations observed in JO201 by MUSE, we found that a good agreement is obtained assuming subsolar values for the metallicity of the warm plasma ($Z = 0.3$–0.5). This result will be analyzed in more detail in a separate paper.

Comprehension of the result obtained in this work, as well as comparing it to results obtained in previous studies, is crucial to determining the direction of future analysis. The emerging scenario is that the interaction between the ICM and the ISM originates in a warm galactic plasma, which is responsible for both the X-ray emission and the [O I]/Hα excess in the optical spectrum. Furthermore, the constraint on the low metallicity of the ionizing plasma provided by our CLOUDY simulations could indicate that the origin of the warm plasma is strictly connected to the ICM. This suggests that the nature of the interaction between the ICM and the ISM is either the cooling of the ICM or the mixing of these two plasmas. On the basis of the results obtained from the radio study of the jellyfish galaxy JO206 (Müller et al. 2021), we speculate that this process could be a direct consequence of the ICM draping and thus that joint radio and X-ray analyses can provide complementary insights on this mechanism. The similarities observed in JW100 and ESO 137-001 (regarding X-ray temperatures, thermal pressure of the surrounding ICM, and, in the case of JO201 and JW100, Mach numbers and excesses of [O I]/Hα) suggest that the emerging mechanism could be a common feature of jellyfish galaxies. Extending the procedure adopted in this paper and in Poggianti et al. (2019b) to other objects of the GASP sample will be crucial for confirming this scenario. We also evince that a better overview on the RPS process could be obtained with both deeper Chandra observations, which provide the opportunity to characterize the thermal properties of jellyfish galaxies, and numerical simulations, which, starting from observational constraints, could allow us to determine the balance between cooling and heating in the ongoing stripping process.

We thank the referee for the useful suggestions that improved the presentation of the work. A.I. thanks C. Stuardi and G. Sabatini for the insightful discussions. Based on observations collected at the European Organization for Astronomical Research in the Southern Hemisphere under ESO program 196.B-0578. This project has received funding from the European Research Council (ERC) under the Horizon 2020 research and innovation program (grant agreement No. 833824). A.I., B.V., and M.G. acknowledge financial contribution from the grant PRIN MIUR 2017 n.20173ML3WW_001 (PI Cimatti). We acknowledge financial contribution from the INAF main-stream funding program (PI Vulcani) and from the agreement ASI-INAF n.2017-14-H.0 (P.I. Moretti). Y.J. acknowledges financial support from CONICYT PAI (Concurso Nacional de Inserción en la Academia 2017) No. 79170132 and FONDECYT Iniciación 2018 No. 11180558. J.F. acknowledges financial support from the UNAM-DGAPA-PAPIIT IA103520 grant, México. A.C.C.L. acknowledges the financial support of the National Agency for Research and Development (ANID) / Scholarship Program / DOCTORADO BECA NACIONAL/2019-21190049.

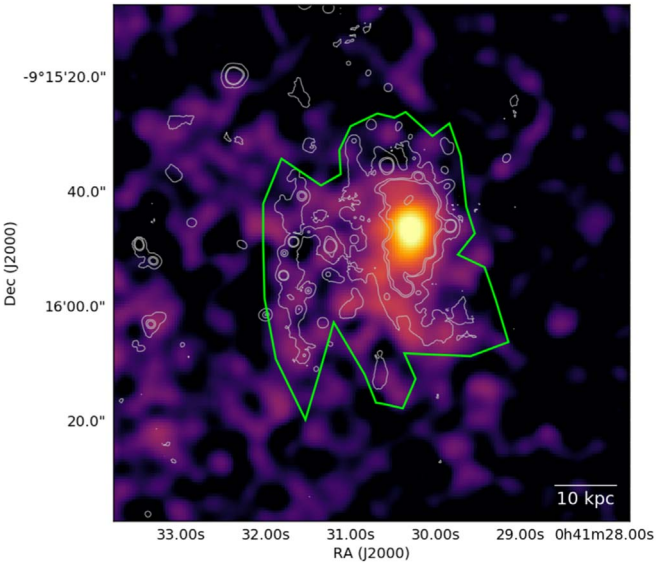

Figure 6. Zoomed-in image of JO201; the region used to extract spectra from the Hα mask is shown in green, while the contour of the Hα emission is shown in silver (Bellhouse et al. 2019), used as reference.

Appendix
Hα Mask

We present here the results of the analysis of the X-ray spectrum extracted in a region resembling the Hα emission (Figure 6). The procedure followed for the extraction and fit of the spectra is the same as that used for the stellar disk mask (see Section 4.2.2). In Table 5 we report the results of the fits obtained combining the galaxy and the additional components as explained in section Section 3.4.2; for two of these models, we fixed the $T_{\rm MAX}$ parameter to the values of the ICM. In particular, model (5), apec+apec, reveals a temperature of $kT = 0.79^{+0.11}_{-0.08}$keV for the galactic component, which is lower than the ICM temperature. A similar result is also obtained with model (6), apec+cemekl, where the $kT_{\rm MAX}$ detected is $kT_{\rm MAX} = 0.9^{+0.3}_{-0.3}$keV, which is lower than the value of the ICM and is compatible with the value found in case (1). For the other two models, (7) apec+cemekl and (8) apec+mkcflow, we set the $T_{\rm MAX}$ parameter to match the temperature of the ICM.

Regarding the metallicity, Z, we note that, when the temperature parameter is free (models (5) and (6)), the Z values obtained are lower than those of the ICM. We considered these values implausible, because the X-ray emitting plasma is either the ICM, or the ISM, or a mixture of these two components; thus, its metallicity is expected to vary between the values of the ICM metallicity ($Z_{\rm ICM} = 0.21$ $Z_{\odot}$, see Section 3.4.2) and those of the ISM metallicity (typical

Table 5
Fit Results for Spectra Extracted from the Hα Mask (Figure 6)

Model	Parameters	χ^2/dof
		χ^2_R
(5) tbabs·(apec+apec)	$kT = 0.79^{+0.11}_{-0.08}$ $Z = 0.07^{+0.05}_{-0.03}$	57.02/49
	$F = (3.4 \pm 0.4)\cdot10^{-14}$ $L = (2.0 \pm 0.2)\cdot10^{41}$	1.164
(6) tbabs·(apec+cemekl)	$kT_{MAX} = 0.9^{+0.3}_{-0.3}$ $\alpha = 0.016^{+3.909}_{-0.017}$	54.67/48
	$Z = 0.06^{+0.05}_{-0.02}$	1.139
	$F = (2.9 \pm 0.3)\cdot10^{-14}$ $L = (1.6 \pm 0.2)\cdot10^{41}$	
(7) tbabs·(apec+cemekl)	$\alpha = 0.01^{+0.27}_{-0.01}$	53.57/49
$kT_{MAX} = 7.1$ keV (fixed)	$Z = 0.4^{+0.5}_{-0.2}$ $F = (2.7 \pm 0.2)\cdot10^{-14}$ $L = (1.3 \pm 0.1)\cdot10^{41}$	1.093
(8) tbabs·(apec+mkcflow)	$kT_{min} = 0.08^{+0.17}_{-0.08}$ $Z = 0.6^{+0.2}_{-0.2}$	67.78/49
$kT_{MAX} = 7.1$ keV (fixed)	$\dot{M} = 2.4^{+3.4}_{-1.0}$ 1.383	
	$F = (6.6 \pm 0.4)\cdot10^{-14}$ $L = (3.19 \pm 0.17)\cdot10^{41}$	

Note. For this region, we resort to the 1B extraction configuration, which models the ICM emission with an additional apec component (see Section 3.4.2). The best-fit parameters shown in the second column refer only to the galactic component indicated in the first column (namely (5) apec, (6) and (7) cemekl, and (8) mkcflow). The unit measures used are: keV for temperature (kT), $Z_\odot$ for metallicity (Z), $M_\odot$ yr^{-1} for the mass accretion rate ($\dot{M}$), erg s^{-1} cm $^{-2}$ for flux (F), and erg s^{-1} for luminosity (L). The unabsorbed flux and luminosity refer only to the galactic component and were measured in the 0.5–10.0 keV energy band.

values are $Z \sim 1\ Z_\odot$). On the contrary, when the temperature is fixed to the value of the ICM ($T_{ICM} = 7.1$ keV, see Section 3.4.2), we reveal plausible values of the metallicity, with $Z = 0.4^{+0.5}_{-0.2}\ Z_\odot$ in model (7) and $Z = 0.6 \pm 0.2\ Z_\odot$ in model (8). This behavior attests to the presence of a temperature–metallicity degeneracy: the statistic at our disposal does not allow us to reliably estimate at the same time both the temperature and the metallicity parameters of the models used in our analysis.

Statistically, it is not possible to discern which emission model is preferred by the fitting procedure because the χ^2_R values obtained from the four fits are acceptable at 68%.

ORCID iDs

M. Giulia Campitiello https://orcid.org/0000-0001-5581-3349
Alessandro Ignesti https://orcid.org/0000-0003-1581-0092
Myriam Gitti https://orcid.org/0000-0002-0843-3009
Fabrizio Brighenti https://orcid.org/0000-0001-9807-8479
Mario Radovich https://orcid.org/0000-0002-3585-866X
Anna Wolter https://orcid.org/0000-0001-5840-9835
Neven Tomičić https://orcid.org/0000-0002-8238-9210
Callum Bellhouse https://orcid.org/0000-0002-6179-8007
Bianca M. Poggianti https://orcid.org/0000-0001-8751-8360
Alessia Moretti https://orcid.org/0000-0002-1688-482X
Benedetta Vulcani https://orcid.org/0000-0003-0980-1499
Yara L. Jaffé https://orcid.org/0000-0003-2150-1130
Rosita Paladino https://orcid.org/0000-0001-9143-6026
Ancla Müller https://orcid.org/0000-0001-9184-7845
Jacopo Fritz https://orcid.org/0000-0002-7042-1965
Ana C. C. Lourenço https://orcid.org/0000-0002-4393-7798
Marco Gullieuszik https://orcid.org/0000-0002-7296-9780

References

Akritas, M. G., & Bershady, M. A. 1996, ApJ, 470, 706
Arnaud, K. A. 1996, in ASP Conf. Ser., 101, Astronomical Data Analysis Software and Systems V, ed. G. H. Jacoby & J. Barnes (San Francisco, CA: ASP), 17
Asplund, M., Grevesse, N., Sauval, A. J., & Scott, P. 2009, ARA&A, 47, 481
Baldwin, J. A., Phillips, M. M., & Terlevich, R. 1981, PASP, 93, 5
Bekki, K., Couch, W. J., & Shioya, Y. 2002, ApJ, 577, 651
Belfiore, F., Maiolino, R., Maraston, C., et al. 2016, MNRAS, 461, 3111
Bellhouse, C., Jaffé, Y. L., Hau, G. K. T., et al. 2017, ApJ, 844, 49
Bellhouse, C., Jaffé, Y. L., McGee, S. L., et al. 2019, MNRAS, 485, 1157
Bellhouse, C., McGee, S. L., Smith, R., et al. 2021, MNRAS, 500, 1285
Boselli, A., Cuillandre, J. C., Fossati, M., et al. 2016, A&A, 587, A68
Calvi, R., Poggianti, B. M., & Vulcani, B. 2011, MNRAS, 416, 727
Consolandi, G., Gavazzi, G., Fossati, M., et al. 2017, A&A, 606, A83
Cowie, L. L., & Songaila, A. 1977, Natur, 266, 501
Ebeling, H., Ma, C.-J., & Barrett, E. 2014, ApJS, 211, 21
Edge, A. C., Stewart, G. C., Fabian, A. C., & Arnaud, K. A. 1990, MNRAS, 245, 559
Edwards, L. O. V., Alpert, H. S., Trierweiler, I. L., Abraham, T., & Beizer, V. G. 2016, MNRAS, 461, 230
Fasano, G., Marmo, C., Varela, J., et al. 2006, A&A, 445, 805
Ferland, G. J., Chatzikos, M., Guzmán, F., et al. 2017, RMxAA, 53, 385
Fielding, D. B., Ostriker, E. C., Bryan, G. L., & Jermyn, A. S. 2020, ApJL, 894, L24
Fossati, M., Fumagalli, M., Boselli, A., et al. 2016, MNRAS, 455, 2028
Fumagalli, M., Fossati, M., Hau, G. K. T., et al. 2014, MNRAS, 445, 4335
Gavazzi, G., Marcelin, M., Boselli, A., et al. 2001, A&A, 377, 745
George, K., Poggianti, B. M., Bellhouse, C., et al. 2019, MNRAS, 487, 3102
George, K., Poggianti, B. M., Gullieuszik, M., et al. 2018, MNRAS, 479, 4126
Gitti, M., Brighenti, F., & McNamara, B. R. 2012, AdAst, 2012, 950641
Gullieuszik, M., Poggianti, B., Fasano, G., et al. 2015, A&A, 581, A41
Gullieuszik, M., Poggianti, B. M., McGee, S. L., et al. 2020, ApJ, 899, 13
Gunn, J. E., Gott, J., & Richard, I. 1972, ApJ, 176, 1
Haffner, L. M., Dettmar, R. J., Beckman, J. E., et al. 2009, RvMP, 81, 969
Haffner, L. M., Reynolds, R. J., & Tufte, S. L. 1999, ApJ, 523, 223
Ho, I. T., Kewley, L. J., Dopita, M. A., et al. 2014, MNRAS, 444, 3894
Ichinohe, Y., Werner, N., Simionescu, A., et al. 2015, MNRAS, 448, 2971
Ignesti, A., Brunetti, G., Gitti, M., & Giacintucci, S. 2020, A&A, 640, A37
Jaffé, Y. L., Poggianti, B. M., Moretti, A., et al. 2018, MNRAS, 476, 4753
Jaffé, Y. L., Smith, R., Candlish, G. N., et al. 2015, MNRAS, 448, 1715
Jaffé, Y. L., Verheijen, M. A. W., Haines, C. P., et al. 2016, MNRAS, 461, 1202
Kalberla, P. M. W., Burton, W. B., Hartmann, D., et al. 2005, A&A, 440, 775
Kanjilal, V., Dutta, A., & Sharma, P. 2021, MNRAS, 501, 1143
Kewley, L. J., Groves, B., Kauffmann, G., & Heckman, T. 2006, MNRAS, 372, 961
Larson, R. B., Tinsley, B. M., & Caldwell, C. N. 1980, ApJ, 237, 692
López-Cruz, O., Añorve, C., Birkinshaw, M., et al. 2014, ApJL, 795, L31
Machacek, M., Nulsen, P., & Stirbat, L. 2005, ApJ, 630, 280
Madsen, G. J., Reynolds, R. J., & Haffner, L. M. 2006, ApJ, 652, 401
Mineo, S., Gilfanov, M., Lehmer, B. D., Morrison, G. E., & Sunyaev, R. 2014, MNRAS, 437, 1698
Mineo, S., Gilfanov, M., & Sunyaev, R. 2012, MNRAS, 426, 1870
Moore, B., Lake, G., & Katz, N. 1998, ApJ, 495, 139
Moretti, A., Gullieuszik, M., Poggianti, B., et al. 2017, A&A, 599, A81
Moretti, A., Paladino, R., Poggianti, B. M., et al. 2020, ApJL, 897, L30
Moretti, A., Poggianti, B. M., Fasano, G., et al. 2014, A&A, 564, A138

Müller, A., Poggianti, B. M., Pfrommer, C., et al. 2021, NatAs, 5, 159
Mushotzky, R. F., & Szymkowiak, A. E. 1988, in NATO Advanced Study Institute (ASI) Series C, Vol. 229, Cooling Flows in Clusters and Galaxies, ed. A. C. Fabian, 53
Nulsen, P. E. J. 1982, MNRAS, 198, 1007
Osterbrock, D. E., & Ferland, G. J. 2006, Astrophysics of Gaseous Nebulae and Active Galactic Nuclei (Melville, NY: Univ. Science Books)
Osterbrock, D. E., & Martel, A. 1992, PASP, 104, 76
Poggianti, B. M., Gullieuszik, M., Tonnesen, S., et al. 2019a, MNRAS, 482, 4466
Poggianti, B. M., Ignesti, A., Gitti, M., et al. 2019b, ApJ, 887, 155
Poggianti, B. M., Jaffé, Y. L., Moretti, A., et al. 2017a, Natur, 548, 304
Poggianti, B. M., Moretti, A., Gullieuszik, M., et al. 2017b, ApJ, 844, 48
Radovich, M., Poggianti, B., Jaffé, Y. L., et al. 2019, MNRAS, 486, 486
Ramatsoku, M., Serra, P., Poggianti, B. M., et al. 2020, A&A, 640, A22
Ranalli, P., Comastri, A., & Setti, G. 2003, A&A, 399, 39
Reynolds, R. J. 1985, ApJ, 294, 256
Reynolds, R. J., Haffner, L. M., & Tufte, S. L. 1999, ApJL, 525, L21
Scannapieco, E., & Brüggen, M. 2015, ApJ, 805, 158
Smith, R. J., Lucey, J. R., Hammer, D., et al. 2010, MNRAS, 408, 1417
Sparre, M., Pfrommer, C., & Ehlert, K. 2020, MNRAS, 499, 4261
Springel, V. 2000, MNRAS, 312, 859
Strickland, D. K., Heckman, T. M., Colbert, E. J. M., Hoopes, C. G., & Weaver, K. A. 2004, ApJ, 606, 829
Sun, M., Donahue, M., Roediger, E., et al. 2010, ApJ, 708, 946
Sun, M., Donahue, M., & Voit, G. M. 2007, ApJ, 671, 190
Sun, M., Jones, C., Forman, W., et al. 2006, ApJL, 637, L81
Sun, M., & Vikhlinin, A. 2005, ApJ, 621, 718
Sutherland, R. S., & Dopita, M. A. 1993, ApJS, 88, 253
Symeonidis, M., Georgakakis, A., Seymour, N., et al. 2011, MNRAS, 417, 2239
Tomičić, N., Vulcani, B., Poggianti, B. M., et al. 2021, ApJ, 907, 22
Tonnesen, S., Bryan, G. L., & Chen, R. 2011, ApJ, 731, 98
Tschöke, D., Bomans, D. J., Hensler, G., & Junkes, N. 2001, A&A, 380, 40
van Gorkom, J. H. 2004, in Clusters of Galaxies: Probes of Cosmological Structure and Galaxy Evolution, ed. J. S. Mulchaey, A. Dressler, & A. Oemler (Cambridge: Cambridge Univ. Press), 305
Veilleux, S., & Osterbrock, D. E. 1987, ApJS, 63, 295
Vollmer, B., Cayatte, V., Balkowski, C., & Duschl, W. J. 2001, ApJ, 561, 708
Vulcani, B., Poggianti, B. M., Gullieuszik, M., et al. 2018, ApJL, 866, L25
Yoon, H., Chung, A., Smith, R., & Jaffé, Y. L. 2017, ApJ, 838, 81
Zhang, B., Sun, M., Ji, L., et al. 2013, ApJ, 777, 122
Zinger, E., Dekel, A., Kravtsov, A. V., & Nagai, D. 2018, MNRAS, 475, 3654